

On the Interplanetary Parameter Schemes which Drive the Variability of the Source/Seed Electron Population at GEO

Christos Katsavrias¹, Sigiava Aminalragia-Giamini², Constantinos Papadimitriou², Ingmar Sandberg², Piers Jiggins³, Ioannis A. Daglis⁴, and Hugh D. Evans⁵

¹University of Athens

²Space Applications and Research Consultancy

³European Space Agency

⁴National and Kapodistrian University of Athens

⁵ESA

November 24, 2022

Abstract

Electron variability at geosynchronous orbit plays a key role in satellite operations especially concerning the low energies which can lead to surface charging effects on spacecraft. In this work, we use 9 years (2011-2019) of electron measurements from GOES-13, 14 and 15 satellites to study the evolution of electron uxes with various solar, solar wind and magnetospheric parameters. The source electron fluxes are shown to be well correlated with AE index and Newell's function, while the seed electron fluxes are shown to be well correlated with solar wind speed. Based on these findings, we have developed a predictive multiple regression model for electron fluxes in the 30-350 keV energy range which uses solely solar wind parameters' measurements. The model may have a variety of applications related nowcasting/forecasting of the distribution of electron fluxes at GEO including serving as low-energy boundary conditions for studying electron acceleration to relativistic energies or providing information for predicting surface and/or internal charging effects on spacecraft.

1 **On the Interplanetary Parameter Schemes which Drive**
2 **the Variability of the Source/Seed Electron Population**
3 **at GEO**

4 **Ch. Katsavrias^{1,2}, S. Amealragia–Giamini^{2,1}, C. Papadimitriou², I.**
5 **Sandberg², P. Jiggins³, I.A. Daglis^{1,4} and H. Evans³**

6 ¹Department of Physics, National and Kapodistrian University of Athens, Greece

7 ²Space Applications and Research Consultancy (SPARC), Athens, Greece

8 ³ESA/ESTEC, Netherlands

9 ⁴Hellenic Space Center, Athens, Greece

10 **Key Points:**

- 11 • Correlation of source electrons at GEO with AE index and seed electrons with so-
12 lar wind speed
- 13 • A multiple regression model is developed for source/seed electron fluxes at GEO
- 14 • The model can successfully predict electron fluxes in the 30–350 keV range.

Corresponding author: Christos Katsavrias, ckatsavrias@phys.uoa.gr

Abstract

Electron variability at geosynchronous orbit plays a key role in satellite operations especially concerning the low energies which can lead to surface charging effects on spacecraft. In this work, we use 9 years (2011–2019) of electron measurements from GOES-13, 14 and 15 satellites to study the evolution of electron fluxes with various solar, solar wind and magnetospheric parameters. The source electron fluxes are shown to be well correlated with AE index and Newell’s function, while the seed electron fluxes are shown to be well correlated with solar wind speed. Based on these findings, we have developed a predictive multiple regression model for electron fluxes in the 30–350 keV energy range which uses solely solar wind parameters’ measurements. The model may have a variety of applications related nowcasting/forecasting of the distribution of electron fluxes at GEO including serving as low-energy boundary conditions for studying electron acceleration to relativistic energies or providing information for predicting surface and/or internal charging effects on spacecraft.

1 Introduction

The variability of the low energy electron population (a few tens to a few hundreds keV), and consequently its prediction, is very important for the inner magnetosphere dynamics for two basic reasons: a) source (≈ 10 – 100 keV) and seed (≈ 100 – 300 keV) electrons act as a ‘reservoir’ which can be further accelerated to relativistic energies (Li et al., 2014; Katsavrias et al., 2019a; Katsavrias et al., 2019b; Daglis et al., 2019; Nasi et al., 2020) and b) are responsible for surface (a few eV to tens of keV) and internal charging (above a few hundred keV) effects on satellites (Baker, 2000; O’Brien & Lemon, 2007; Thomsen et al., 2013; Zheng et al., 2019).

Over the past few years, several studies have attempted comparisons of electron fluxes at geosynchronous orbit (mostly focused on relativistic electrons) with various solar wind parameters, with the ultimate goal of obtaining a predictive capability for the electron population variability for a given set of solar wind input parameters.

Shi et al. (2009) used GEO-LANL measurements during 2000–2003 to study the relationship of low-energy and relativistic electrons to magnetospheric compression (in terms of elevated solar wind pressure). They concluded that the primary response of 50–75 keV electrons is an increase in flux, while that of relativistic electrons is a decrease in flux. Li et al. (2005) used five years (1995–1999) of measurements of LANL electron flux at geosynchronous orbit, to show that the solar wind speed is the most important controlling parameter of the electron population variability. The authors further stated that the dependence on solar wind conditions varies with electron energy, with <200 keV responding more to the polarity of the Interplanetary Magnetic Field (IMF) which, in turn, leads to enhanced substorm activity, and magnetospheric convection associated with the azimuthal electric field. Kellerman and Shprits (2012), used LANL data for a period spanning over 20 years to show that the low-energy fluxes exhibit a positive correlation with solar wind speed and density, while mid-to-high energy electron fluxes are anti-correlated with density.

Moreover, Sillanpää et al. (2017) analyzed five years (2011–2015) of GOES-13/MAGED measurements to conclude that solar wind speed has a moderate correlation with the 30–200 keV electrons, while IMF B_z has a significant influence, especially, in the 0 to 12 Magnetic Local Time (MLT) sector. Furthermore, they used the aforementioned statistics to develop an empirical prediction model for energies 30–200 keV driven by these parameters.

The purpose of this paper is to reveal the interplanetary parameters which are best correlated with low-energy electron radiation environment at GEO, but also, to introduce a new approach in creating a predictive model for source/seed electrons. The lat-

65 ter is achieved by using only solar wind and interplanetary magnetic field (IMF) param-
 66 eters and no geomagnetic or magnetospheric indices. This approach is two-folded since
 67 the solely use of solar wind parameters a) allows the physical interpretation of the model
 68 in terms reconnection and the magnetic flux transferred in the magnetosphere and b)
 69 allows the nowcasting/forecasting capability since solar wind parameters' measurements
 70 (in contrast with geomagnetic indices) are provided in near-real time.

71 2 Datasets

72 The Geostationary Operational Environmental Satellite system (GOES) consists
 73 of several satellites in geosynchronous orbit (GEO). For this study, GOES-13, 14 and 15
 74 were selected due to the existence of the MAGnetospheric Electron Detector (MAGED)
 75 which provides electron flux measurements in five energy channels of 30–50 keV, 50–100
 76 keV, 100–200 keV, 200–350 keV, and 350–600 keV. The MAGED instrument consists
 77 of nine collimated solid state detectors for each energy range. Each detector provides uni-
 78 directional electron differential fluxes (FEDU) depending on the look direction of each
 79 detector. Following Rodriguez (2014), we exploit the magnetic field vector's measure-
 80 ments from the fluxgate magnetometers on-board GOES to calculate the respective pitch
 81 angles. Then, we perform a numerical integration of the uni-directional fluxes in the pitch
 82 angle distribution over $0 < PA < 180$ degrees. In order to achieve a sufficient numer-
 83 ical convergence for the integration, the uni-directional fluxes are binned into 64 bins
 84 with a resolution of 2.8125 degrees and proceed to the numerical integration. We per-
 85 form the calculations of omni-directional differential electron fluxes (FEDO-1/cm².sec.
 86 keV) only in the cases that we have in our disposal at least three of the five uni-directional
 87 (FEDU) measurements.

Table 1. Description of the coupling functions used in this study.

Name	Functional Form	Description	Reference
Half-Wave Rectifier	$HWR = V_{SW} \cdot B_S$	Corresponds to the rate of the dayside reconnection	Burton et al. (1975)
Epsilon parameter	$\epsilon = V_{SW} \cdot B^2 \cdot \sin^4 \frac{\theta_c}{2}$	Describes the Poynting flux incident at the magnetopause	Akasofu (1981)
Wygant's function	$E_{WAV} = V_{SW} \cdot B_{TAN} \cdot \sin^4 \frac{\theta_c}{2}$	Similar to Epsilon	Wygant et al. (1983)
Kan and Lee's function	$E_{KL} = V_{SW} \cdot B_{TAN} \cdot \sin^2 \frac{\theta_c}{2}$	Similar to Epsilon	Kan and Lee (1979)
Newell's function	$\frac{d\phi}{dt} = V_{SW}^{4/3} \cdot B_{TAN}^{2/3} \cdot \sin^{8/3} \frac{\theta_c}{2}$	Proportional to the rate at which magnetic flux is opened at the magnetopause	Newell et al. (2007)

88 The dataset also includes 1-min resolution measurements of the solar wind and ge-
 89 omagnetic parameters available by the OMNIWeb service of the Space Physics Data Fa-
 90 cility at the Goddard Space Flight Center (<http://omniweb.gsfc.nasa.gov/>, provided as
 91 propagated values at the nose of the magnetopause). The solar wind parameters include:

- 92 • the interplanetary magnetic field (IMF) along with its three components (Bx, By
 93 and Bz) in Geocentric Solar Magnetospheric (GSM) coordinates,

- 94 • the southward magnetic field (B_s), which corresponds to the absolute negative val-
95 ues of B_z when all positive values have been set to zero, and the azimuthal elec-
96 tric field at the magnetopause (E_y),
- 97 • the solar wind flow speed (V_{sw}), dynamic pressure (P_{sw}), temperature (T) and
98 numerical density (N),
- 99 • the geomagnetic indices Dst, AE, Kp and Ap.

100 Finally, additional calculations of coupling functions are also used and are summa-
101 rized in table 1. These coupling functions are widely used (by several studies) and are
102 shown to be able of making predictions about how the solar wind could interact with the
103 magnetosphere, in terms of correlating with geomagnetic indices.

104 3 Correlation Analysis

105 For the performed correlation analysis, we have used the calculated omni-directional
106 differential electron fluxes with 5-min resolution and keep only those measurements which
107 initially were found at near-equatorial pitch angles ($a_{eq} > 75$ deg). This was done in order
108 to restrict the investigation to measurements of near-equatorial mirroring particles
109 which correspond to the majority of the population and, moreover, are less affected by
110 pitch angle scattering effects (Usanova et al., 2014). The electron fluxes, the solar wind
111 parameters and the geomagnetic indices measurements, as well as the coupling functions
112 calculations were grouped into 3-hour bins and from each bin the mean and the 95th quan-
113 tile (hence forward Q95) were derived. Using these statistical parameters the relation-
114 ships between electron fluxes and the selected parameters are investigated using Pear-
115 son’s correlation coefficient.

116 Below we highlight the results of the investigation for the three variables that ex-
117 hibited the highest correlations. We define as high correlation the ones with correlation
118 coefficients (hence forward CCs) higher than 0.5.

119 Figure 1, shows the Pearson’s CCs of 3-hour mean and Q95 values of electron flux
120 as a function of energy with three parameters: solar wind speed, AE index and Newell’s
121 coupling function. As shown, there is a strong correlation of the two lower energy chan-
122 nels of GOES/MAGED (central energies at 40 and 75 keV) with the AE index (middle
123 panel) as the CCs of both the mean and Q95 are in the 0.6–0.7 range. This result clearly
124 indicates the dependence of the source (approximately in the 10–100 keV energy range)
125 electron population at GEO on the substorm activity as it is expressed by the AE in-
126 dex. As we move to higher electron energies, the solar wind speed becomes significantly
127 more important (left panel) with the corresponding CCs being at least on the 0.5 thresh-
128 old. This indicates that the seed (approximately in the 100–350 keV energy range) elec-
129 trons are not purely substorm driven but rather depend on the enhanced convection driven
130 by the fast solar wind and/or the enhanced ULF driven inward diffusion. Note that the
131 150 keV channel of MAGED seems to be the transition point between the aforementioned
132 mechanisms. In detail, the average of 150 keV electron flux (mean) is better correlated
133 with solar wind speed while, during extreme cases (Q95), is better correlated with AE
134 index. Finally, figure 1 shows a relatively good correlation of the source electron flux at
135 GEO with the Newell’s function which is somehow expected since the latter is found to
136 be well correlated with the former (Newell et al., 2007). As already mentioned in table
137 1, Newell’s function is proportional to the rate at which magnetic flux is opened at the
138 magnetopause, which in turn is linked with the magnetic tension stored in the magne-
139 totail and, consequently, the triggering of substorm injections. We note here that the use
140 of geomagnetic indices such as the AE index, even though it exhibits very good corre-
141 lations with the electron flux at GEO, is not practical for forecasting/nowcasting as it
142 is not available in real time. Nevertheless, the use of a proxy for the magnetic flux at the
143 magnetopause (such as $d\phi/dt$) which is a function of solar wind speed, IMF and its ori-
144 entation may prove a valuable tool.

Figure 1. Pearson's CCs between 3-hour values of the electron flux with three parameters as a function of energy: (left) solar wind speed, (middle) AE index and (right) Newell's coupling function. Black and red stars correspond to the Pearson's correlation coefficients of the mean and 95th quantile values, respectively.

145 4 Multiple Regression Model

146 4.1 Methodology and Regression Evaluation

147 Using 9 years, 2011–2019, of MAGED data from GOES-13, 14 and 15 we have de-
 148 veloped a multiple regression model for source/seed electron fluxes at GEO. We note that
 149 these years span the maximum and declining phase of SC 24 (2008–2019), capturing its
 150 largest part and therefore a statistically important part of the expected variability in GEO.
 151 Our main goal is to develop a viable and reliable nowcasting/forecasting model for the
 152 low energy part of the electron population. We have used a multiple regression approach
 153 which can account for the relationships and correlation trends discussed above. Addi-
 154 tionally this approach allows for the evaluation of the influence of each variable in tan-
 155 dem with all other variables.

156 The mathematical formulation for the multiple regression model is shown below
 157 in equation 1. It consists of a linear combination of the natural logarithms of four vari-
 158 ables (V_{sw} , P_{sw} , IMF and eBs) and the squares of the logarithms with an intercept
 159 and a modifying factor which contains the MLT dependence.

Figure 2. Cross-plots of 3-hour mean MAGED electron flux versus the electron fluxes given by the multiple regression model at 40, 75, 150, 275 and 475 keV. The solid blue line corresponds to $y=x$ and the dashed green lines correspond to $y=2\cdot x$ and $y=x/2$. The dashed red lines correspond to $y=4\cdot x$ and $y=x/4$. Dataset spans the whole 2011–2019 time-period.

$$J = e^{c_1 \cdot sMLT + c_2 \cdot cMLT + c_0} \cdot P_{SW}^{\alpha_1 + \beta_1 \cdot \ln(P_{SW})} \cdot eBs^{\alpha_2 + \beta_2 \cdot \ln(eBs)} \cdot V_{SW}^{\alpha_3 + \beta_3 \cdot \ln(V_{SW})} \cdot IMF^{\alpha_4 + \beta_4 \cdot \ln(IMF)} \quad (1)$$

160 where $sMLT = \sin(15 \cdot MLT)$, $cMLT = \cos(15 \cdot MLT)$ and eBs is the exponen-
 161 tial of Bs which was used here because it allows for the derivation of results even when
 162 the Bs variable has a value of zero and it was empirically found that the regression was
 163 slightly improved.

164 In detail, the regression model consists of an exponential which contains the MLT
 165 dependence (which is important since we use 3-hour averages which correspond to 3 hour
 166 bins in MLT) and the product of power laws of the four variables with added feedback
 167 terms in the power index—in the form of the natural logarithm of the variables themselves—
 168 multiplied by a constant. This essentially creates a product of variable power laws and
 169 the reason for selecting this formulation and its effects are discussed in detail further on
 170 below. We note here that our model is in the same spirit as other existing coupling func-
 171 tions such as the Newell function (Newell et al., 2007), the Epsilon parameter (Akasofu,
 172 1981), the Half-wave Rectifier (Burton et al., 1975), and more, shown in table 1. Such
 173 functions have been widely used in many studies and in essence aim to perform similar
 174 tasks as the goal of this work; to describe the variability of the interaction of the solar
 175 wind with the magnetosphere by using products of power laws of solar wind parameters
 176 such as the solar wind speed, the tangential component of the IMF, and the solar wind
 177 clock angle ($\theta_c = \arctan(B_y/B_z)$).

178 Figure 2 shows the cross-plots for the 3-hour mean of the MAGED electron flux
 179 values—including all dataset values—against the electron fluxes given by our model for the
 180 five energy channels (40, 75, 150, 275, and 475 keV). We note here that in order to ob-
 181 tain optimum results (in terms of the best regression scores) we used a shifted dataset
 182 corresponding to time-lags of: (a) 3 hours for the two lowest GOES/MAGED energy chan-
 183 nels (40 and 75 keV), (b) 15 hours for the 150 keV channel and (c) 21 hours for the two
 184 highest channels (275 and 475 keV). It is seen that the vast majority of the regressed val-
 185 ues fall within a factor of four (red dashed lines) of the data and mostly cluster along
 186 the equality line in blue, while a significant fraction of them do not exceed a factor of
 187 two. Moreover, the regressed values exhibit a different behavior depending on the en-
 188 ergy channel. In detail, the model seems to underestimate the highest flux values at the
 189 first two energy channels by a factor of two (green dashed lines). On the other hand, the
 190 model overestimates the lower flux values at the 275 and 475 keV channels. Such out-
 191 liers occur mostly in the tails at the cross-plots for values close to the background while
 192 the fluxes of high intensities are regressed well forming narrow noses along the equality
 193 lines.

194 We note that the electrons of the highest MAGED channel have an energy of 475
 195 keV transitioning into the relativistic regime. Even though such electrons are not con-
 196 sidered source/seed it is interesting to observe that the regression is relatively compa-
 197 rable with the much lower energy of 275 keV, well within the seed population typical en-
 198 ergy limits. This indicates that the approach we employ can account (within the lim-
 199 itations of the model) for a significant part of the electron flux variability even up to this
 200 energy. However, we also note that we would consider this the upper energy limit of our
 201 approach.

202 Table 2 lists the free parameters for the mean 3-hour values with their intervals at
 203 95% confidence level, the mean absolute percentage error (MAPE) and the percentage
 204 of empirical estimated values which are within the factor-of-2 and factor-of-4 limits. As
 205 shown, the mean absolute percentage error (MAPE) is less than 100% concerning the
 206 first four energy channels and only at the highest channel (475 keV) reaches $\approx 133\%$,
 207 meaning that—on average—the estimated flux values differ from the measured ones less
 208 than a factor of two. Finally, more than 72% and 94% of the regressed values of the first
 209 four channels fall within a factor of two and four of the data, respectively.

210 These results show that the model performs overall well and is able to successfully
 211 regress the electron fluxes at GEO. The Q95 values (see also figure S1 and table S1 in
 212 the supplementary material) exhibit very similar results meaning that both the average
 213 and high values for electron fluxes at GEO can be successfully regressed.

Table 2. Coefficients of the Regression Model and the corresponding 95% confidence levels for the 3-hour mean MAGED electron fluxes at GEO. MAPE stands for the mean absolute percentage error of the regression analysis, while Ratio 2 and 4 correspond to the percentage of empirical estimated values which are within the factor-of-2 and factor-of-4 limits, respectively.

E (keV)	40	75	150	275	475
c_0	-32.18 [-37.52 , -26.85]	-34.28 [-39.58 , -28.97]	-56.93 [-66.43 , -51.43]	-84.08 [-90.52 , -77.63]	-88.64 [-96.54 , -80.75]
c_1	0.35 [0.34 , 0.36]	0.18 [0.17 , 0.19]	0.03 [0.02 , 0.04]	-0.05 [-0.07 , -0.04]	-0.10 [-0.42 , -0.39]
c_2	-0.11 [-0.12 , -0.10]	-0.20 [-0.21 , -0.19]	-0.27 [-0.28 , -0.26]	-0.34 [-0.36 , -0.33]	-0.40 [-0.11 , -0.08]
α_1	0.20 [0.18 , 0.22]	0.10 [0.08 , 0.12]	-0.07 [-0.09 , -0.05]	-0.26 [-0.28 , -0.23]	-0.42 [-0.45 , -0.39]
α_2	0.32 [0.31 , 0.33]	0.21 [0.20 , 0.22]	0.17 [0.16 , 0.18]	0.15 [0.14 , 0.16]	0.14 [0.13 , 0.16]
α_3	12.10 [10.34 , 13.86]	12.48 [10.73 , 14.23]	19.61 [17.80 , 21.43]	27.68 [25.55 , 29.80]	28.14 [25.54 , 30.75]
α_4	0.79 [0.69 , 0.89]	0.64 [0.54 , 0.73]	0.21 [0.11 , 0.31]	-0.24 [-0.36 , -0.12]	-0.60 [-0.75 , -0.46]
β_1	-0.09 [-0.11 , -0.08]	-0.08 [-0.10 , -0.07]	0.02 [0.006 , 0.04]	0.07 [0.06 , 0.09]	0.08 [0.06 , 0.10]
β_2	-0.02 [-0.01 , -0.008]	-0.01 [-0.01 , -0.009]	-0.01 [-0.03 , -0.01]	-0.007 [-0.008 , -0.006]	-0.005 [-0.007 , -0.004]
β_3	-0.81 [-1.55 , -1.25]	-0.82 [-0.97 , -0.68]	-1.40 [-1.66 , -0.48]	-2.01 [-2.18 , -1.83]	-1.99 [-2.20 , -1.77]
β_4	-0.20 [-0.23 , -0.17]	-0.17 [-0.20 , -0.14]	-0.04 [-0.07 , -0.01]	0.03 [-0.002 , 0.07]	0.07 [0.03 , 0.12]
MAPE (%)	54.0	55.9	61.6	89.4	133.7
Ratio 2 (%)	76.4	78.3	78.2	72.2	61.9
Ratio 4 (%)	97.1	97.0	96.3	94.1	89.9

214

4.2 Validation and Prediction Capabilities

215

216

217

218

219

220

221

While a successful regression is a strong indication of the validity of the model it does not guarantee that it can produce good results outside a regression scheme, i.e. when used in a predictive capacity, which is the goal in this work. For this purpose we use annual fractions of the 9-year dataset to validate our approach. An iterative "leave-one-out" validation process is employed in which the flux values which are predicted are not used in the regression. The process has been used to validate regression models in similar scenarios, e.g. Aminalragia-Giamini et al. (2020), and is detailed below:

222

223

1. The algorithm defines a specific year and isolates the corresponding 3-hour measurements of flux, solar wind speed and pressure, IMF and Bs.

Figure 3. Validation cross-plots of 3-hour mean MAGED electron flux versus the electron fluxes predicted by the multiple regression model at 40 keV per year using the iterative "leave-one-out" validation process. The solid blue line corresponds to $y=x$ and the dashed red lines correspond to $y=2\cdot x$ and $y=x/2$. The mean absolute percentage error for each iteration is included in the title of each panel.

- 224 2. The algorithm then performs the multiple regression with the rest of the dataset,
 225 using the formula expanded in equation 1. For example, if we consider the year
 226 2011, the regression will be made using the measurements from the 2012–2019 time
 227 period.
- 228 3. The model derived in the previous step is then used to predict the fluxes of the
 229 excluded year using the solar wind, pressure, IMF and Bs respective values that
 230 were also excluded from the regression.
- 231 4. The process repeats iteratively for all the available years in the dataset.

232 This process allows the derivation of true predictions for each and every year in our
 233 dataset.

As shown in figure 3, the predicted fluxes at 40 keV agree well with the majority of measurements clustering along the $y = x$ equality lines in blue and remaining almost always within a factor of 2 (dashed red lines above and below). Moreover, the MAPE spans the 45–60% range which is consistent with the 54% value which corresponds to the full regression. The only exception is the year 2018 during which there is always a tail in the cross-plots for values close to the background which consequently increases the MAPE. This behavior during 2018 is exhibited in 75 and 150 keV energy channels as well (see also figures S3 and S4 in the supplementary material).

Concerning the two higher energy channels at 275 and 475 keV (see also figures S5 and S6 in the supplementary material) the years 2011, 2013 and 2014 exhibit also elevated MAPE values which are also attributed to tails in the cross-plots for values close to the background. The fact that the model systematically overestimates the extremely low flux values at the higher energies indicates that it cannot account for extreme and abrupt losses (e.g. magnetopause shadowing). The latter is also supported by the fact that the aforementioned years coincide with years of extreme solar activity.

Figure 4 shows the cross-plots for the 3-hour mean of the MAGED electron flux values—including all dataset values—against the electron fluxes predicted by our model for the five energy channels (40, 75, 150, 275, and 475 keV) using the "leave-one-out" process. As shown, the predicted electron flux values exhibit the same features with the regressed ones (figure 2). Once again, the predictions seem to slightly underestimate the highest flux values at the first two energy channels by a factor of two, while they significantly overestimate the lower flux values at the 275 and 475 keV channels. The similarities between the regressed and predicted electron flux values are also imprinted in the calculated MAPE values of the later which exhibit insignificant differences compared to the former. These insignificant differences suggest that the variations between the free parameters of the predicted and regressed values are also insignificant. The Q95 values (see also figure S6 in the supplementary material) exhibit very similar results meaning that both the prediction capabilities of the model are successful in both the mean and Q95 values.

The aforementioned results indicate that the model has an overall successful prediction which seems to be mostly unaffected by the SC phase, and thus, the intensity of the geospace disturbances. Moreover, it is shown that the model performs well in a predictive capacity and is able to predict within a relatively small range the average and 95th quantile values of the electron differential fluxes at GEO over a wide range of solar wind conditions spanning many years and the largest part of a solar cycle.

5 Discussion and Conclusions

Taking advantage of 9 years of measurements of electron fluxes at GEO we have investigated in depth the influence of several solar wind and magnetospheric parameters on their variability. A correlation analysis indicated several parameters that drive the source electron population (30–100 keV) with the most important being substorm activity (in terms of AE index). The high CC values between source electron fluxes and AE index indicate that the emergence of this population is always linked to the substorm activity (Li et al., 2005). The correlation of source/seed electrons with AE index is also shown to be strong at the outer radiation belt by Smirnov et al. (2019). As we move to higher energies (seed electrons of >100 keV), the correlation of flux with the AE index decreases but, at the same time, the solar wind speed becomes more important. This feature indicates that, in contrast with the source population, seed electrons are not purely substorm driven. Enhanced solar wind speed is responsible for the generation of ULF waves which—combined with enhanced convection—can further accelerate substorm injected particles (see also Kellerman and Shprits (2012) and Jaynes et al. (2015) and references therein).

Figure 4. Cross-plots of 3-hour mean MAGED electron flux versus the electron fluxes predicted by the model at 40, 75, 150, 275 and 475 keV using the "leave-one-out" process. The solid blue line corresponds to $y=x$ and the dashed green lines correspond to $y=2\cdot x$ and $y=x/2$. The dashed red lines correspond to $y=4\cdot x$ and $y=x/4$. The mean absolute percentage error is included in the title of each panel. Dataset spans the whole 2011–2019 time-period.

285 Based on this 9-years dataset and the aforementioned results we have developed
 286 and validated a multiple regression model for 30–350 keV electron fluxes at GEO. The
 287 idea is to express substorm activity, which in turn affects the variability of electrons at
 288 GEO, as a function of solar wind parameters in the spirit of already existing coupling
 289 functions. From a physics point of view, the mathematical formulation of the model ex-
 290 presses the variability of electron flux at GEO as the result of the opened magnetic flux
 291 at the magnetopause, which in turn triggers substorm activity. This is achieved by a com-
 292 bination of four factors: the rate of convection toward the magnetopause (V_{sw}), the prob-
 293 ability that there will be reconnection and its strength (B_s) and the strength of the IMF
 294 (which corresponds to the amount of flux opened) while P_{sw} is a correction factor (MLT
 295 is discussed further on). The input from these factors is shifted at specific time-lags de-
 296 pending on the energy channel. The aforementioned time-lag is proven quite important

297 since it allows the model to have predictive capabilities using near real-time solar wind
 298 measurements. The model predicts quite successfully the distribution of electron fluxes
 299 of GOES/MAGED at the 30–350 keV energy range with MAPE values between the pre-
 300 dicted and measured values in the 50–60% range. Furthermore, the majority of the pre-
 301 dicted flux values (70–80%) differ no more than a factor of 2 from the respective mea-
 302 sured ones. Nevertheless, as we approach the relativistic electrons lower limit (part of
 303 channel 4 corresponds to relativistic electron energy) the model exhibits tails in the cross-
 304 plots for values close to the background. Such cases may be related with intense losses
 305 due to magnetopause shadowing and/or pitch angle scattering effects (Jaynes et al., 2015;
 306 Li et al., 2016) which, the model, cannot account for.

307 The numerical values of the free parameters allow the explanation of the mathe-
 308 matical formulation in the regression model we have implemented. As discussed previ-
 309 ously, due to the feedback terms the power indices in equation 1 are variable as they in-
 310 corporate feedback from the physical variable itself in the form of its natural logarithm.
 311 This allows the power indices to take positive and negative values and thus capture in
 312 one mathematical formulation both the positive and negative correlations of the phys-
 313 ical variables with the electron fluxes at all the energies.

314 This is particularly important for the Psw and IMF variables which exhibit a trend
 315 of diminishing correlation transitioning to anti-correlation as the electron energy becomes
 316 higher. Figure 5 shows all the values of the power law indices for the four parameters
 317 used in the model at the five energies. It can be seen that for the first two channels (black
 318 and blue solid lines) the indices are mostly positive and therefore capture the positive
 319 correlation of the four parameters to the electron fluxes. The indices of the last two chan-
 320 nels exhibit different behavior depending on the parameter. The indices of Vsw and eBs
 321 are always positive, while the indices of IMF and Psw are mostly negative and capture
 322 the anti-correlation with the variables. The third channel is an in-between case here hav-
 323 ing both positive and negative values. The negative power law indices of Psw and IMF
 324 are probably related with loss processes such as magnetopause shadowing which in turn
 325 is known to be energy dependent. As shown, the higher the electron energy the more neg-
 326 ative the power law index becomes (cyan and red lines). Another interesting feature is
 327 the contribution of the solar wind speed index to each energy channel. As shown, the
 328 index has always greater values for increasing energy channel which means that speed
 329 becomes more important for higher energy electrons. This result is consistent with the
 330 initial correlation analysis and the fact that convection is more important for seed elec-
 331 trons.

332 Finally, the use of the modifying factor which contains the MLT dependence is based
 333 on the averaged flux distribution as a function of MLT. As shown in the upper panel of
 334 figure 6, the averaged (over all the full dataset) flux distribution of the first two energy
 335 channels exhibit a sinusoidal profile as a function of MLT, while the the rest of them ex-
 336 hibit a rather normal distribution. The profile of the MLT index (lower panel) aims at
 337 reproducing this exact feature.

338 Keeping in mind the points discussed, our conclusions concerning the parameter
 339 schemes which drive the source/seed electron variability at GEO are the following:

- 340 1. Source electron (10–100 keV) fluxes at GEO are primarily driven by substorm ac-
 341 tivity (in terms of AE index), while seed electron (100–350 keV) fluxes are mostly
 342 driven by solar wind speed.
- 343 2. The developed regression model can successfully predict the 3-hour average and
 344 Q95 of source/seed electron fluxes in the 30–350 keV energy range.
- 345 3. The model may have a variety of applications related to nowcasting/forecasting
 346 of the distribution of electron fluxes at GEO (e.g. serve as low-energy boundary
 347 conditions for studying electron acceleration to relativistic energies or provide in-
 348 formation for predicting surface and/or internal charging effects on spacecraft).

Figure 5. Power law indices as a function of the natural logarithm of each parameter used by the model: (top left) Psw, (top right) eBs, (bottom left) Vsw and (bottom right) IMF. Black, blue, green, red and cyan solid lines correspond to the 40, 75, 150, 275 and 475 keV, respectively.

Acknowledgments

This work is supported by ESA's Science Core Technology Programme (CTP) under contract No. 4000127282/19/IB/gg. NOAA GOES data can be found at <https://satdat.ngdc.noaa.gov/sem/goes/data/>.

References

- Akasofu, S. I. (1981, June). Energy coupling between the solar wind and the magnetosphere. , *28*(2), 121-190. doi: 10.1007/BF00218810
- Aminalragia-Giamini, S., Jiggins, P., Anastasiadis, A., Sandberg, I., Aran, A., Vainio, R., . . . Dierckxsens, M. (2020, December). Prediction of Solar Proton Event Fluence spectra from their Peak flux spectra. *Journal of Space Weather and Space Climate*, *10*, 1. doi: 10.1051/swsc/2019043
- Baker, D. N. (2000, December). The occurrence of operational anomalies in space-

Figure 6. (Upper panel) The normalised averaged flux as a function of MLT for the 5 GOES/MAGED energy channels. (Lower panel) The MLT index as a function of MLT. Black, blue, green, red and cyan solid lines correspond to the 40, 75, 150, 275 and 475 keV, respectively.

- craft and their relationship to space weather. *IEEE Transactions on Plasma Science*, 28(6), 2007-2016. doi: 10.1109/27.902228
- Burton, R. K., McPherron, R. L., & Russell, C. T. (1975). An empirical relationship between interplanetary conditions and dst. *Journal of Geophysical Research (1896-1977)*, 80(31), 4204-4214. doi: 10.1029/JA080i031p04204
- Daglis, I. A., Katsavrias, C., & Georgiou, M. (2019, July). From solar sneezing to killer electrons: outer radiation belt response to solar eruptions. *Philosophical Transactions of the Royal Society of London Series A*, 377(2148), 20180097. doi: 10.1098/rsta.2018.0097
- Jaynes, A. N., Baker, D. N., Singer, H. J., Rodriguez, J. V., Loto'aniu, T. M., Ali, A. F., ... Reeves, G. D. (2015, September). Source and seed populations for relativistic electrons: Their roles in radiation belt changes. *Journal of Geophysical Research (Space Physics)*, 120(9), 7240-7254. doi: 10.1002/2015JA021234
- Kan, J. R., & Lee, L. C. (1979). Energy coupling function and solar wind-magnetosphere dynamo. *Geophysical Research Letters*, 6(7), 577-580. doi: 10.1029/GL006i007p00577
- Katsavrias, C., Daglis, I. A., & Li, W. (2019a). On the Statistics of Acceleration and Loss of Relativistic Electrons in the Outer Radiation Belt: A Superposed Epoch Analysis. *Journal of Geophysical Research (Space Physics)*, 124(4), 2755-2768. doi: 10.1029/2019JA026569
- Katsavrias, C., Sandberg, I., Li, W., Podladchikova, O., Daglis, I., Papadimitriou, C., ... Aminiara-Giamini, S. (2019b). Highly relativistic electron flux enhancement during the weak geomagnetic storm of april-may 2017. *Journal of Geophysical Research: Space Physics*, 124(6), 4402-4413. doi:

- 386 10.1029/2019JA026743
- 387 Kellerman, A. C., & Shprits, Y. Y. (2012). On the influence of solar wind conditions
388 on the outer-electron radiation belt. *Journal of Geophysical Research: Space*
389 *Physics*, 117(A5). doi: 10.1029/2011JA017253
- 390 Li, W., Ma, Q., Thorne, R. M., Bortnik, J., Zhang, X.-J., Li, J., ... Goldstein, J.
391 (2016). Radiation belt electron acceleration during the 17 march 2015 geomag-
392 netic storm: Observations and simulations. *Journal of Geophysical Research:*
393 *Space Physics*, 121(6), 5520-5536. doi: 10.1002/2016JA022400
- 394 Li, W., Thorne, R. M., Ma, Q., Ni, B., Bortnik, J., Baker, D. N., ... Claudepierre,
395 S. G. (2014, June). Radiation belt electron acceleration by chorus waves
396 during the 17 March 2013 storm. *Journal of Geophysical Research (Space*
397 *Physics)*, 119(6), 4681-4693. doi: 10.1002/2014JA019945
- 398 Li, X., Baker, D. N., Temerin, M., Reeves, G., Friedel, R., & Shen, C. (2005,
399 April). Energetic electrons, 50 keV to 6 MeV, at geosynchronous orbit:
400 Their responses to solar wind variations. *Space Weather*, 3(4), 04001. doi:
401 10.1029/2004SW000105
- 402 Nasi, A., Daglis, I., Katsavrias, C., & Li, W. (2020). Interplay of source/seed
403 electrons and wave-particle interactions in producing relativistic elec-
404 tron psd enhancements in the outer van allen belt. *Journal of Atmo-*
405 *spheric and Solar-Terrestrial Physics*, 105405. Retrieved from [http://](http://www.sciencedirect.com/science/article/pii/S1364682620302133)
406 www.sciencedirect.com/science/article/pii/S1364682620302133 doi:
407 <https://doi.org/10.1016/j.jastp.2020.105405>
- 408 Newell, P. T., Sotirelis, T., Liou, K., Meng, C. I., & Rich, F. J. (2007, January).
409 A nearly universal solar wind-magnetosphere coupling function inferred from
410 10 magnetospheric state variables. *Journal of Geophysical Research (Space*
411 *Physics)*, 112(A1), A01206. doi: 10.1029/2006JA012015
- 412 O'Brien, T. P., & Lemon, C. L. (2007, March). Reanalysis of plasma measure-
413 ments at geosynchronous orbit. *Space Weather*, 5(3), 03007. doi: 10.1029/
414 2006SW000279
- 415 Rodriguez, J. V. (2014). Goes 13-15 mage/pd pitch angles, algorithm theoretical ba-
416 sis document, version 1.0. *NOAA NESDIS NGDC*.
- 417 Shi, Y., Zesta, E., & Lyons, L. R. (2009, February). Features of energetic parti-
418 cle radial profiles inferred from geosynchronous responses to solar wind dy-
419 namic pressure enhancements. *Annales Geophysicae*, 27(2), 851-859. doi:
420 10.5194/angeo-27-851-2009
- 421 Sillanpää, I., Ganushkina, N. Y., Dubyagin, S., & Rodriguez, J. V. (2017, Decem-
422 ber). Electron Fluxes at Geostationary Orbit From GOES MAGED Data.
423 *Space Weather*, 15(12), 1602-1614. doi: 10.1002/2017SW001698
- 424 Smirnov, A. G., Kronberg, E. A., Latallerie, F., Daly, P. W., Aseev, N., Shprits,
425 Y. Y., ... Taylor, M. G. G. T. (2019, April). Electron Intensity Measurements
426 by the Cluster/RAPID/IES Instrument in Earth's Radiation Belts and Ring
427 Current. *Space Weather*, 17(4), 553-566. doi: 10.1029/2018SW001989
- 428 Thomsen, M. F., Henderson, M. G., & Jordanova, V. K. (2013, May). Statistical
429 properties of the surface-charging environment at geosynchronous orbit. *Space*
430 *Weather*, 11(5), 237-244. doi: 10.1002/swe.20049
- 431 Usanova, M. E., Drozdov, A., Orlova, K., Mann, I. R., Shprits, Y., Robertson,
432 M. T., ... Wygant, J. (2014, March). Effect of EMIC waves on relativistic
433 and ultrarelativistic electron populations: Ground-based and Van Allen Probes
434 observations. , 41(5), 1375-1381. doi: 10.1002/2013GL059024
- 435 Wygant, J. R., Torbert, R. B., & Mozer, F. S. (1983, July). Comparison
436 of S3-3 polar cap potential drops with the interplanetary magnetic field
437 and models of magnetopause reconnection. , 88(A7), 5727-5735. doi:
438 10.1029/JA088iA07p05727
- 439 Zheng, Y., Ganushkina, N. Y., Jiggins, P., Jun, I., Meier, M., Minow, J. I., ...
440 Kuznetsova, M. M. (2019, October). Space Radiation and Plasma Effects on

441 Satellites and Aviation: Quantities and Metrics for Tracking Performance of
442 Space Weather Environment Models. *Space Weather*, 17(10), 1384-1403. doi:
443 10.1029/2018SW002042

Figure 1.

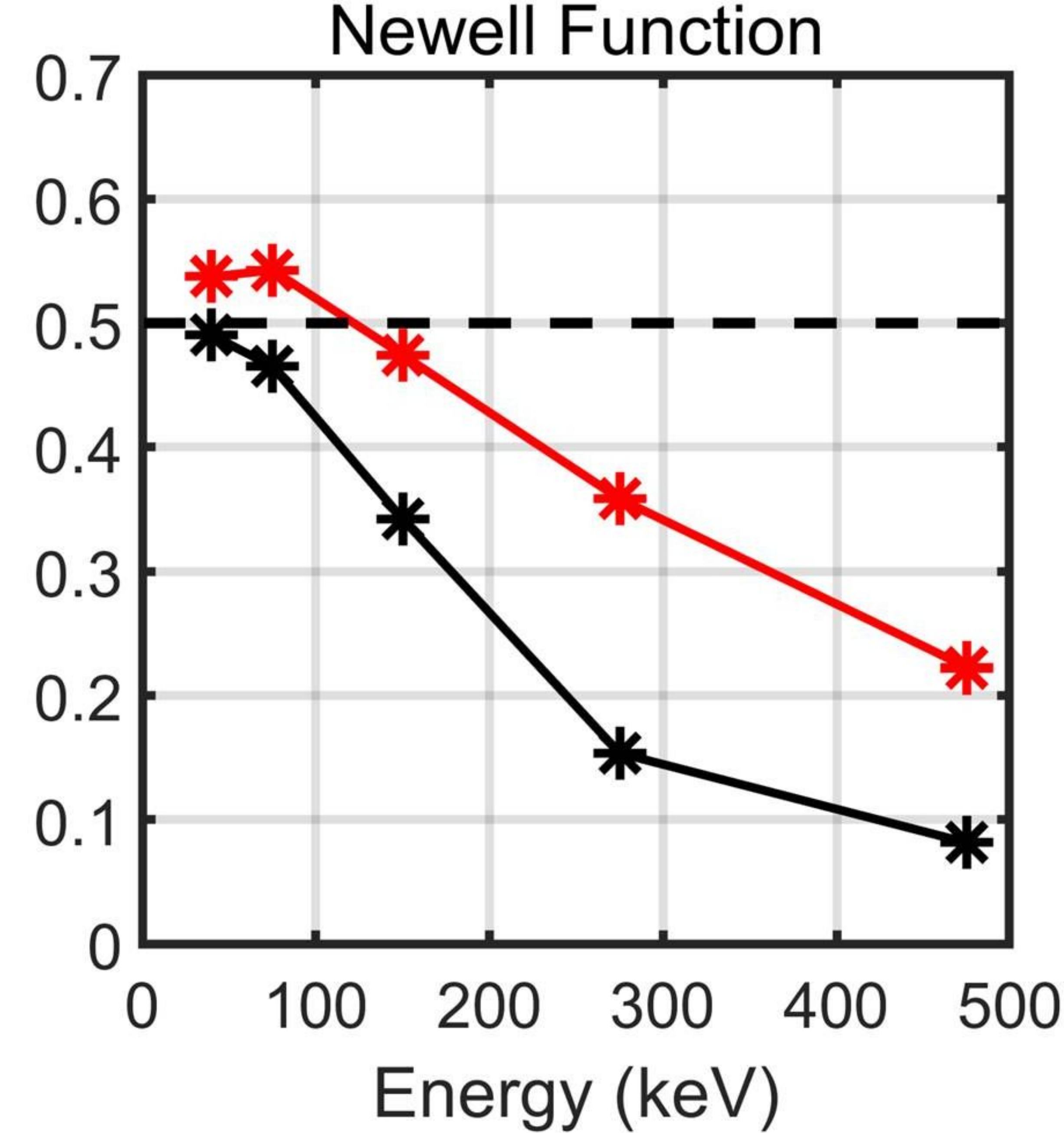
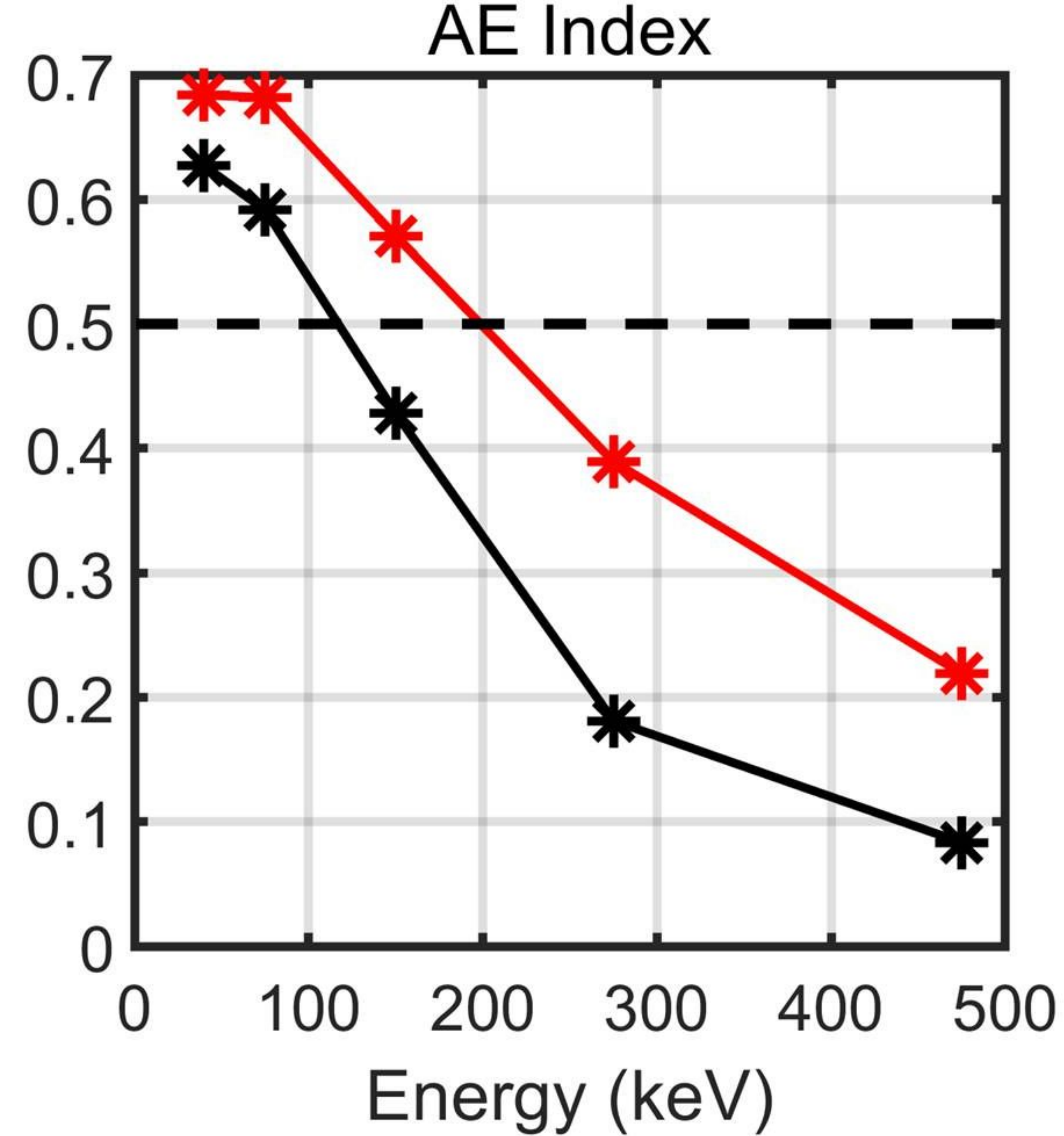
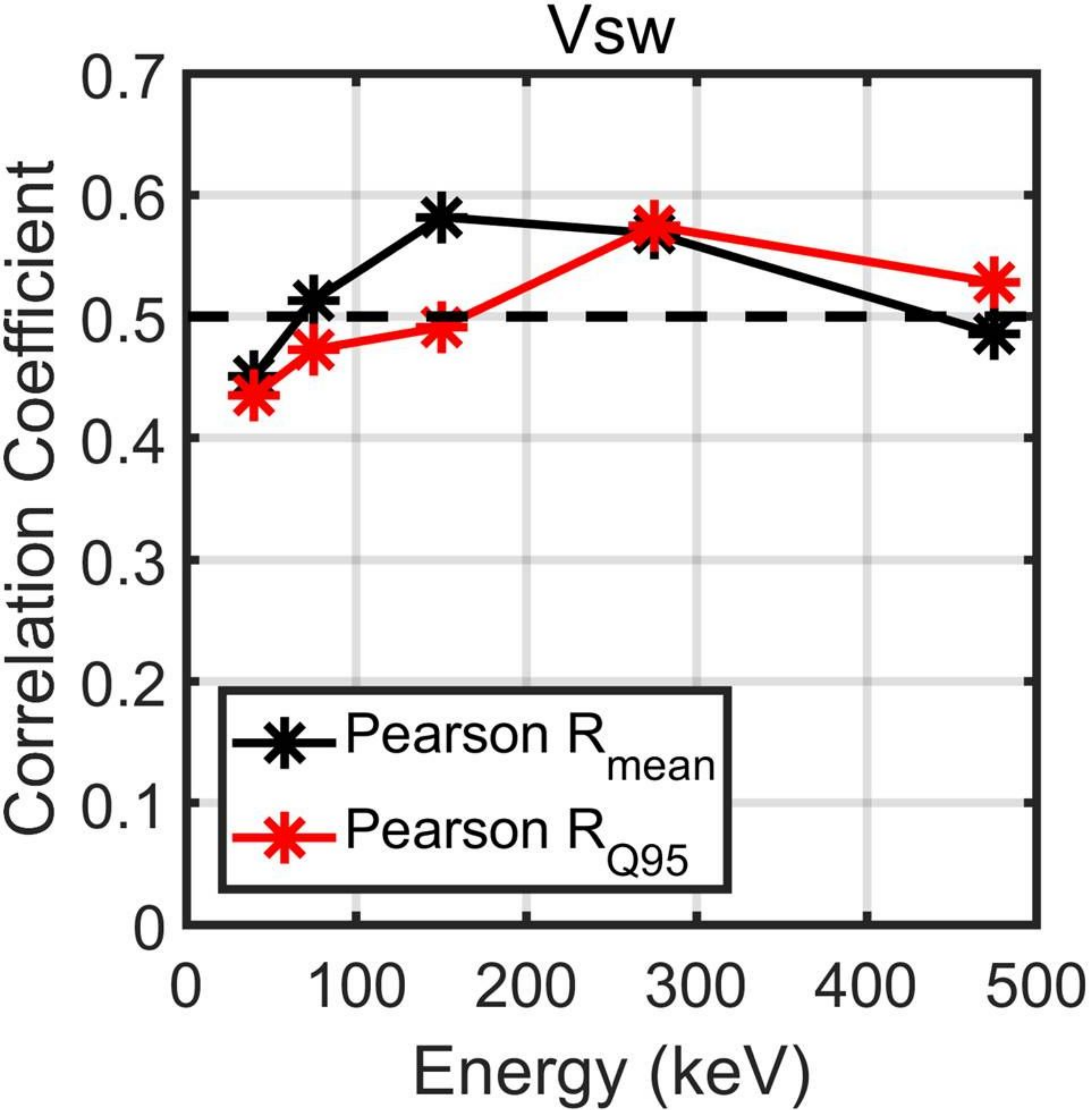


Figure 2.

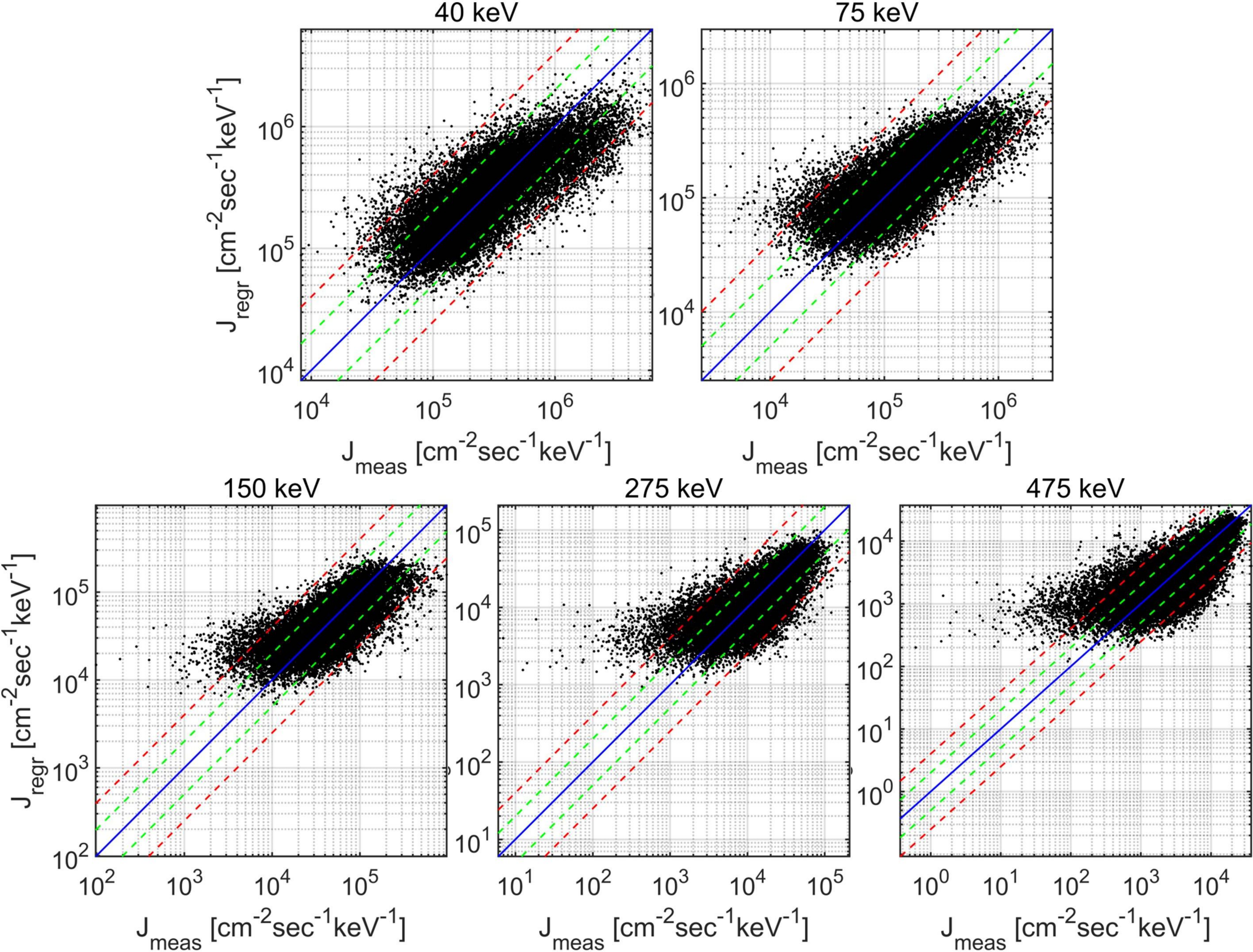


Figure 3.

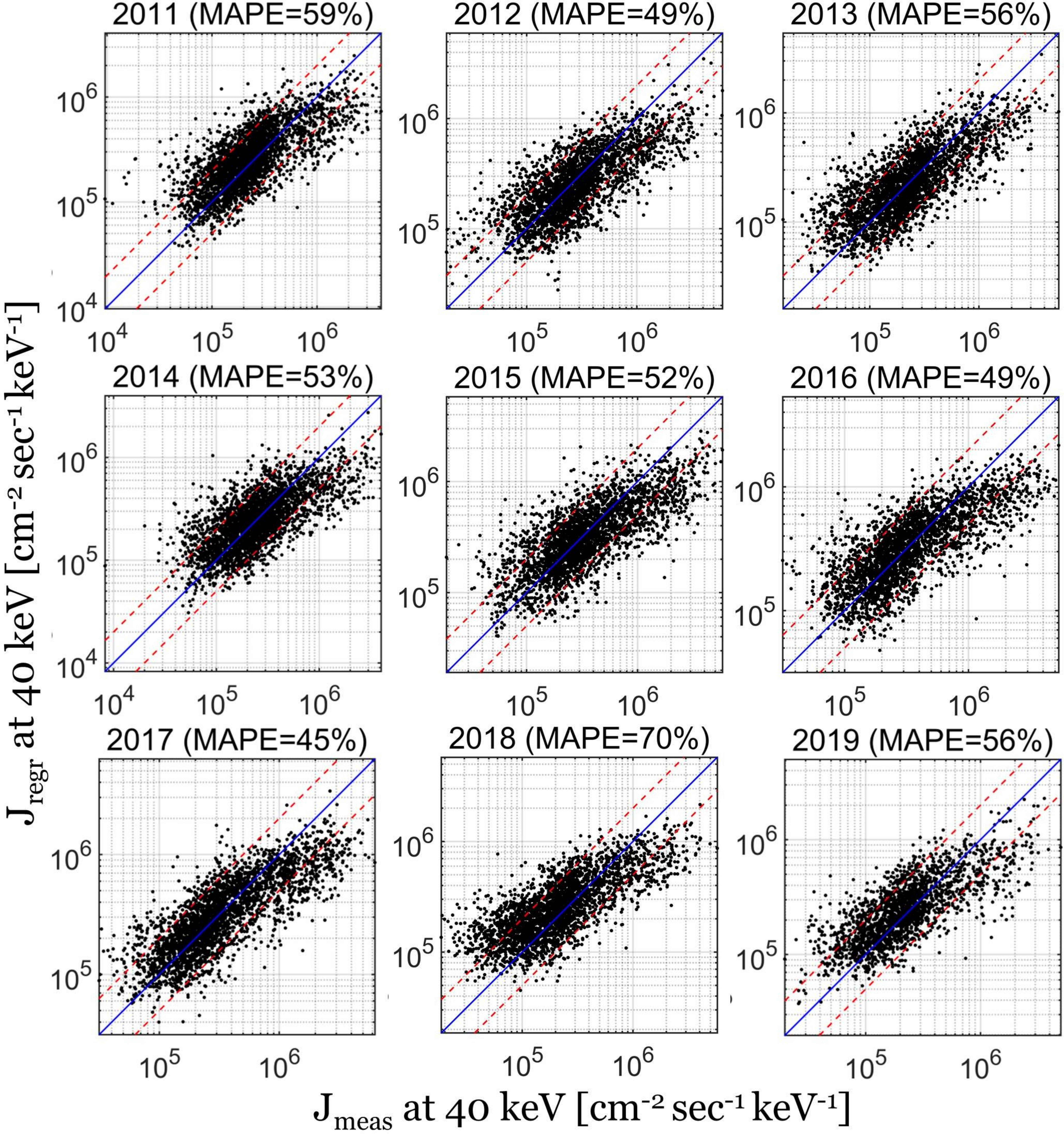


Figure 4.

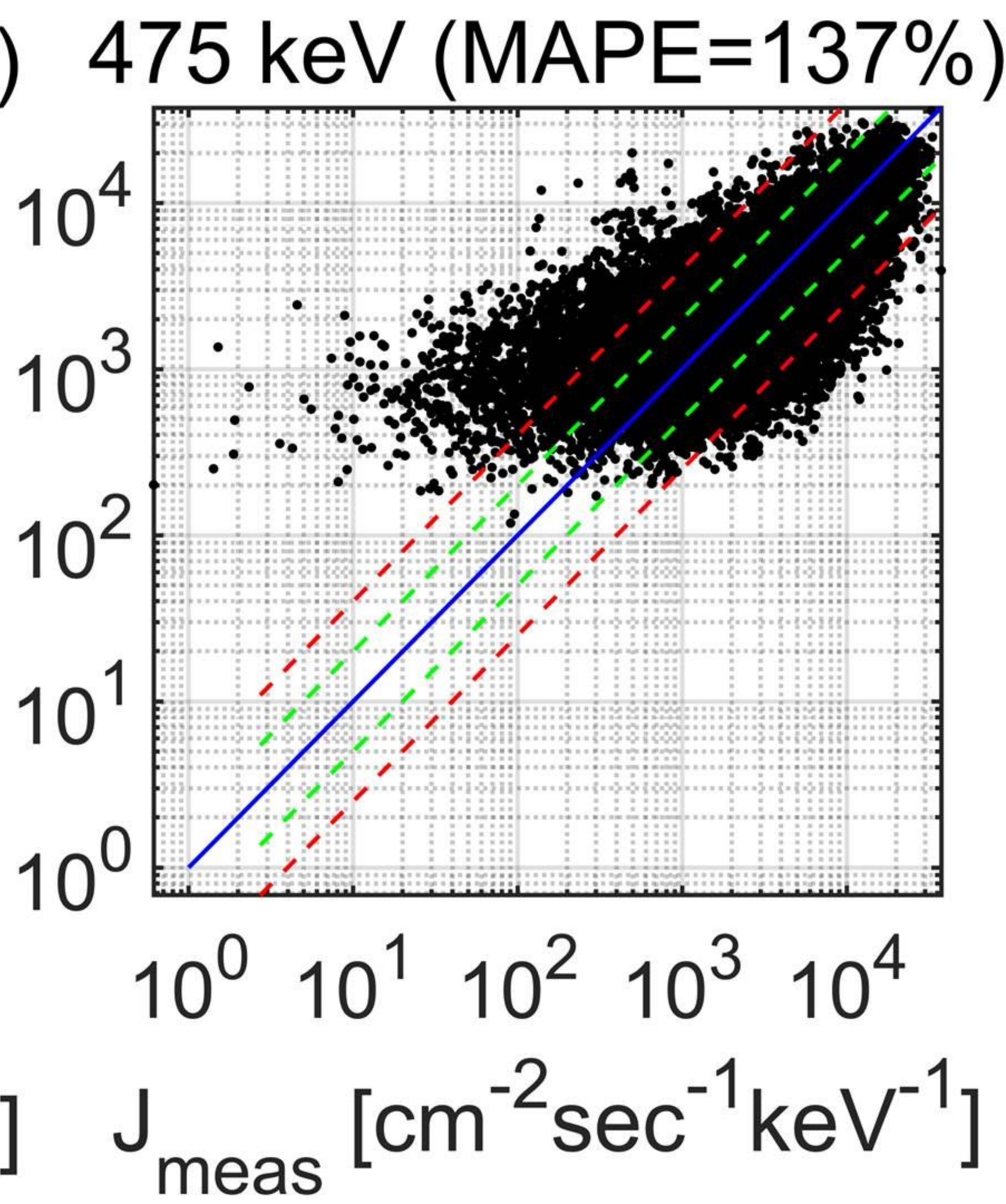
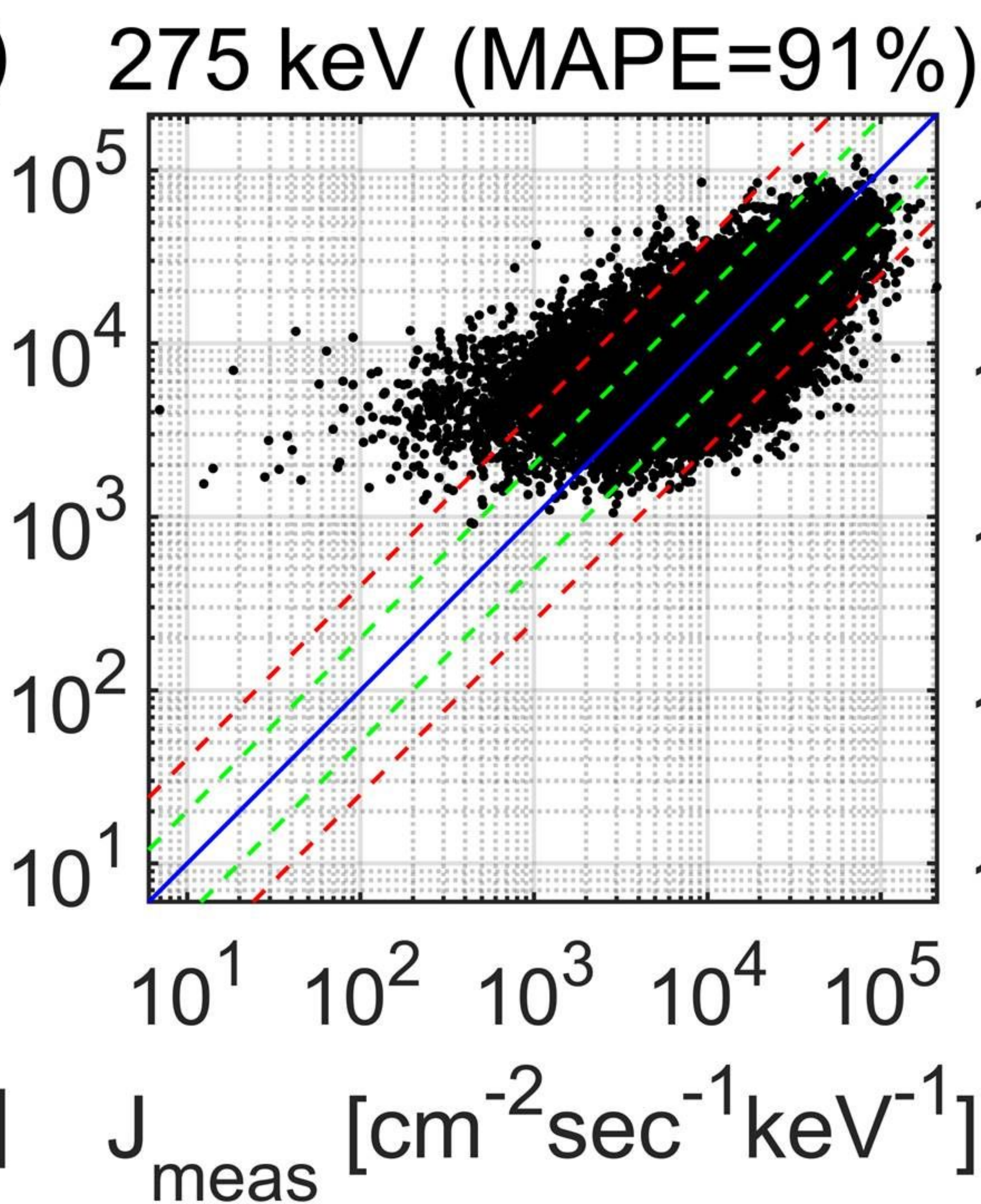
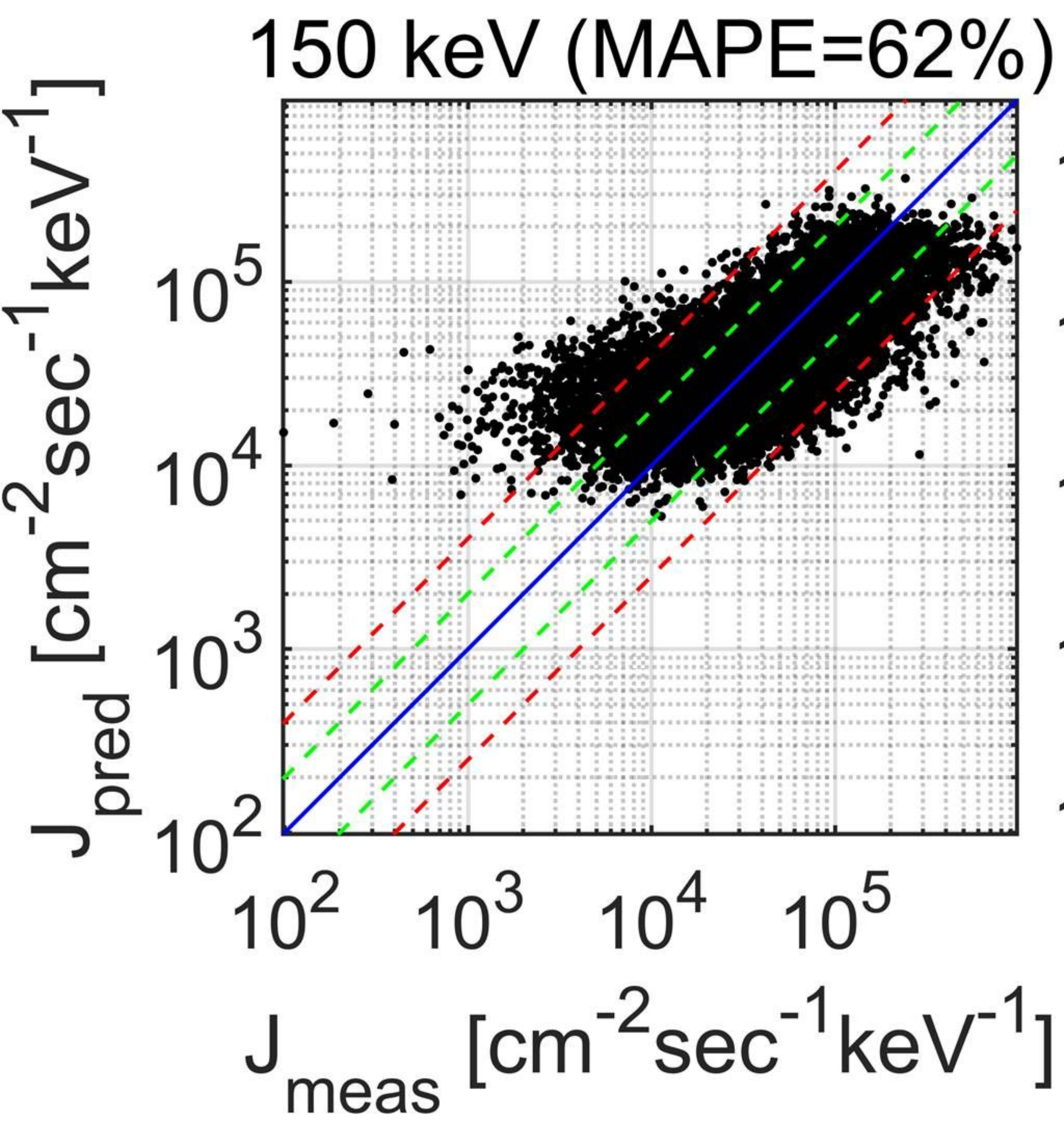
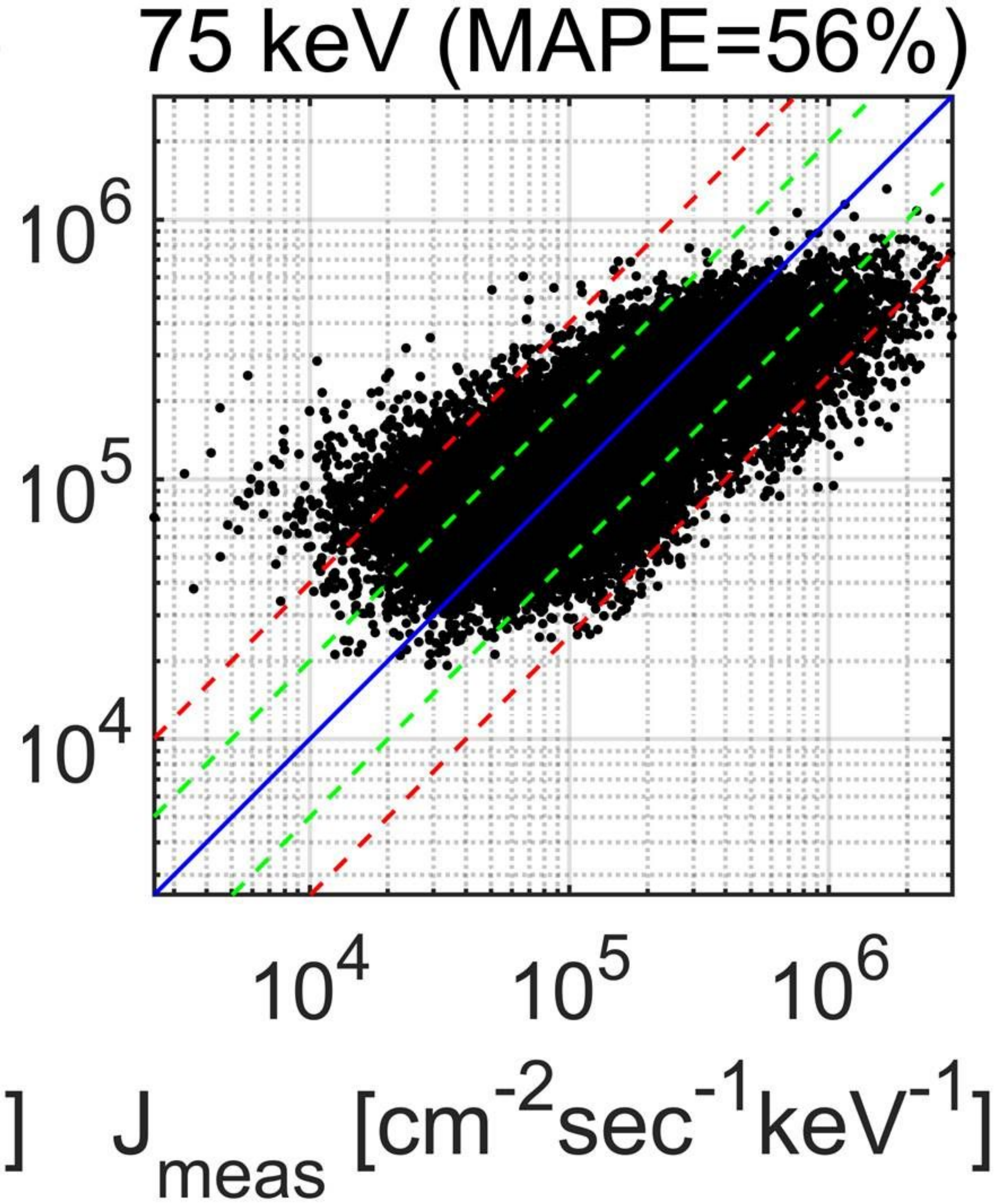
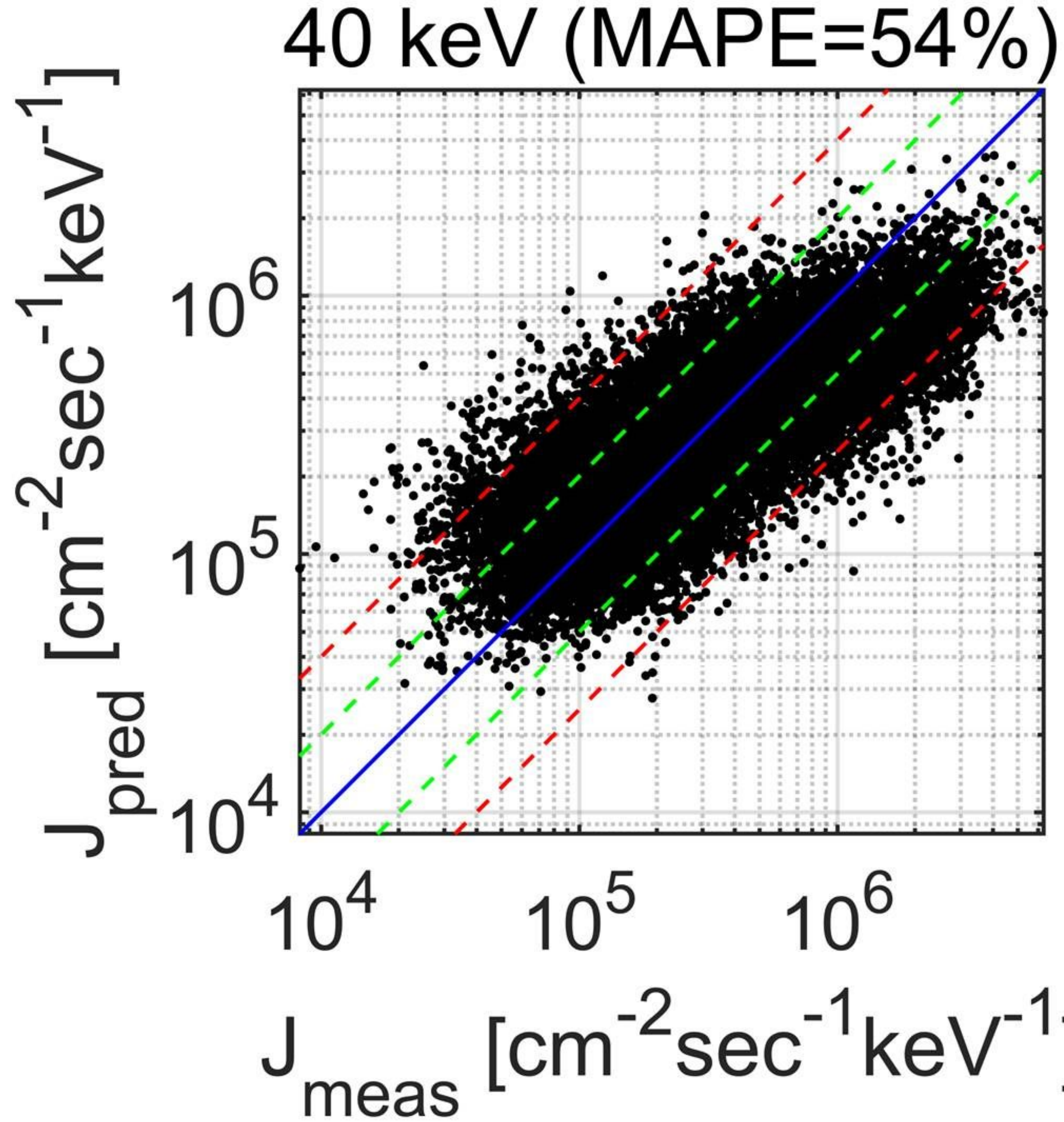


Figure 5.

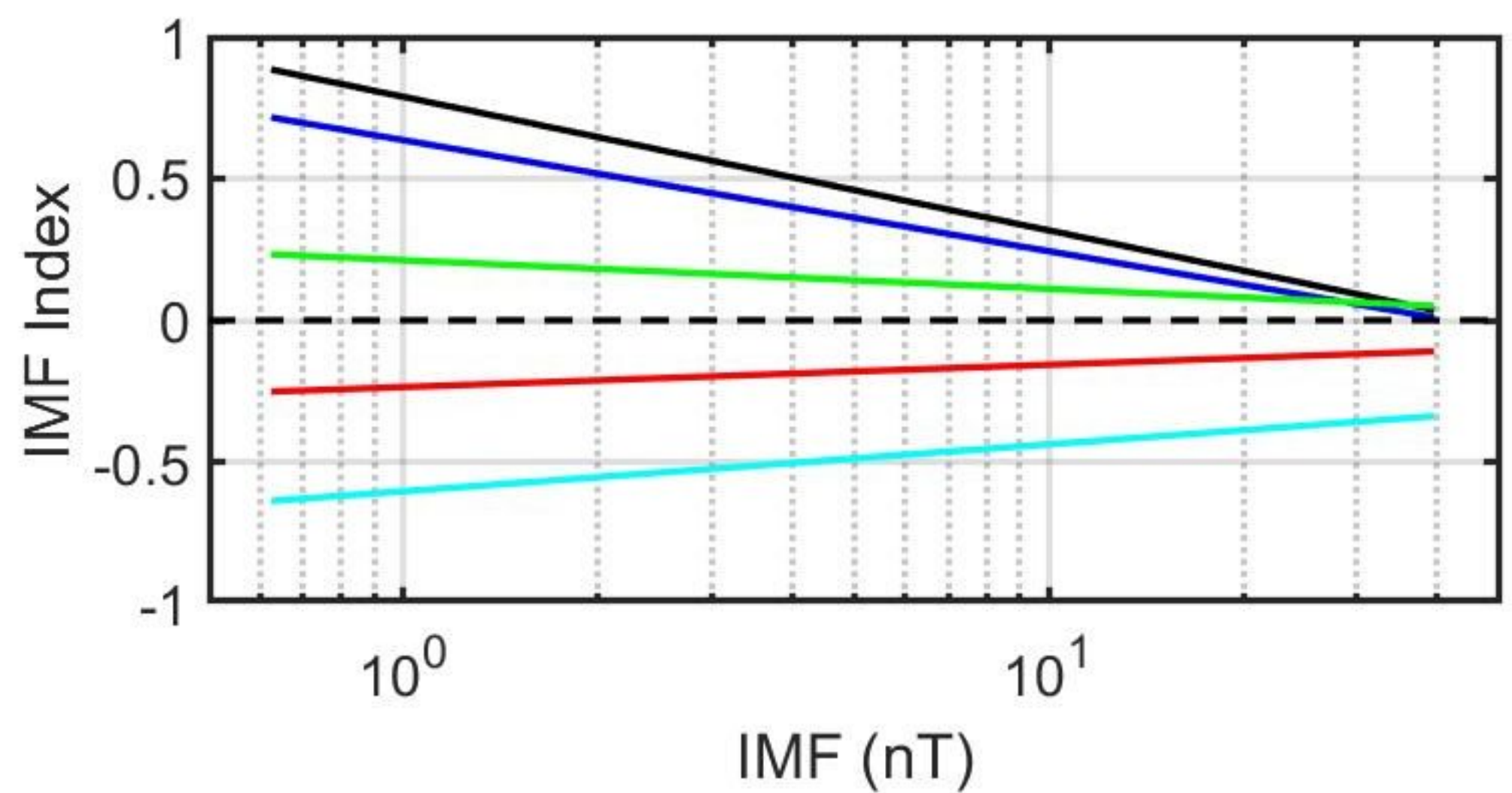
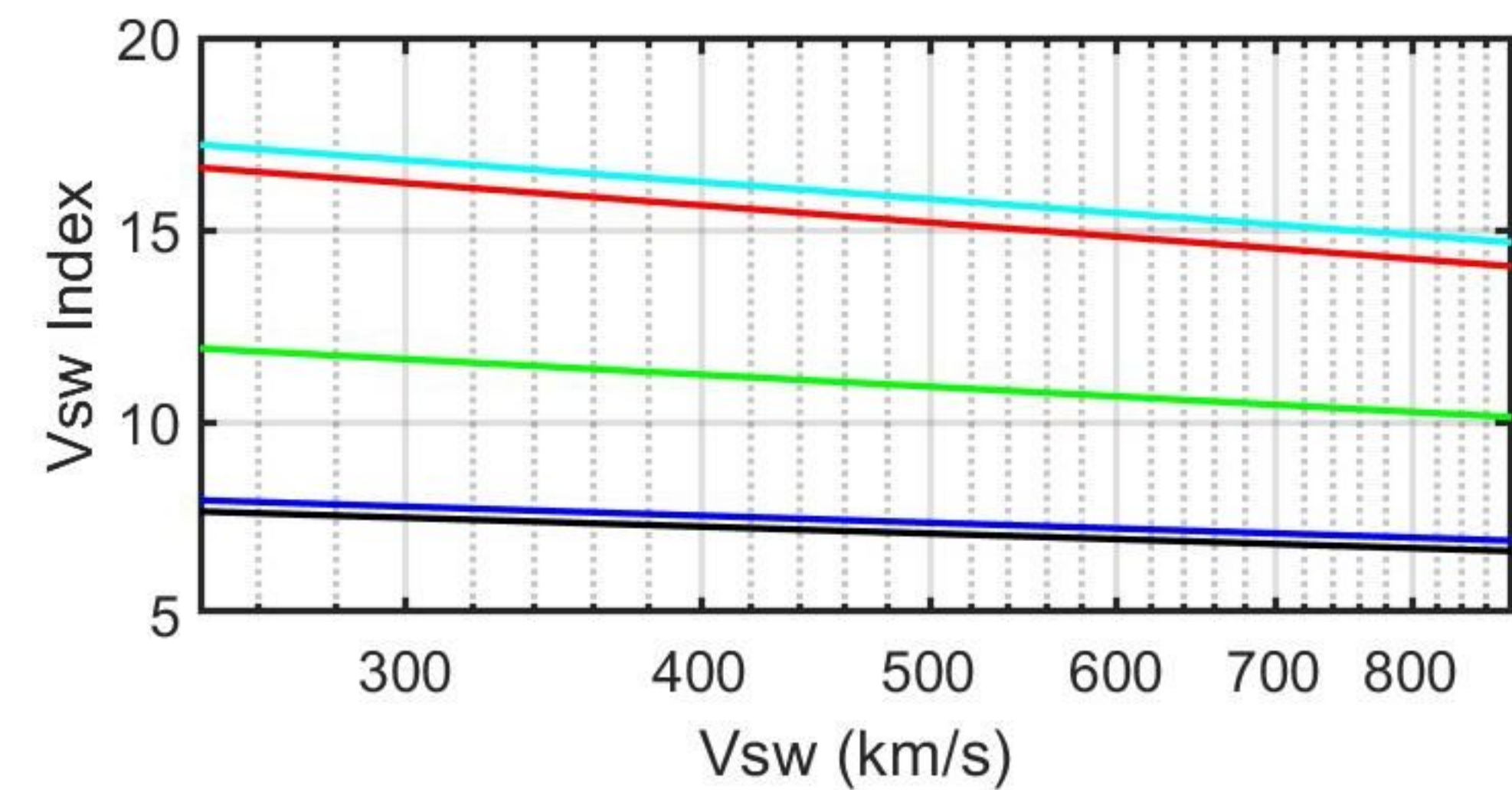
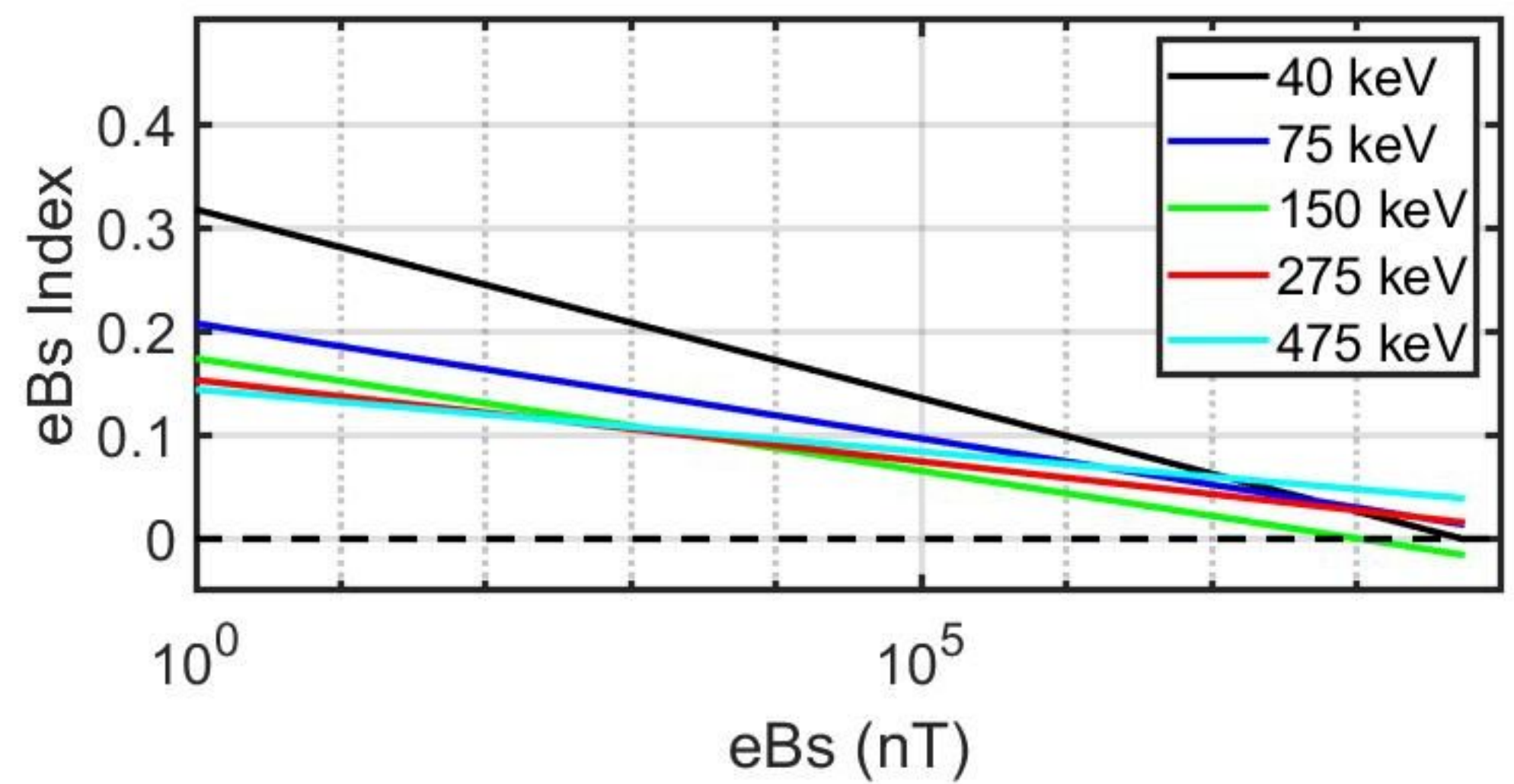
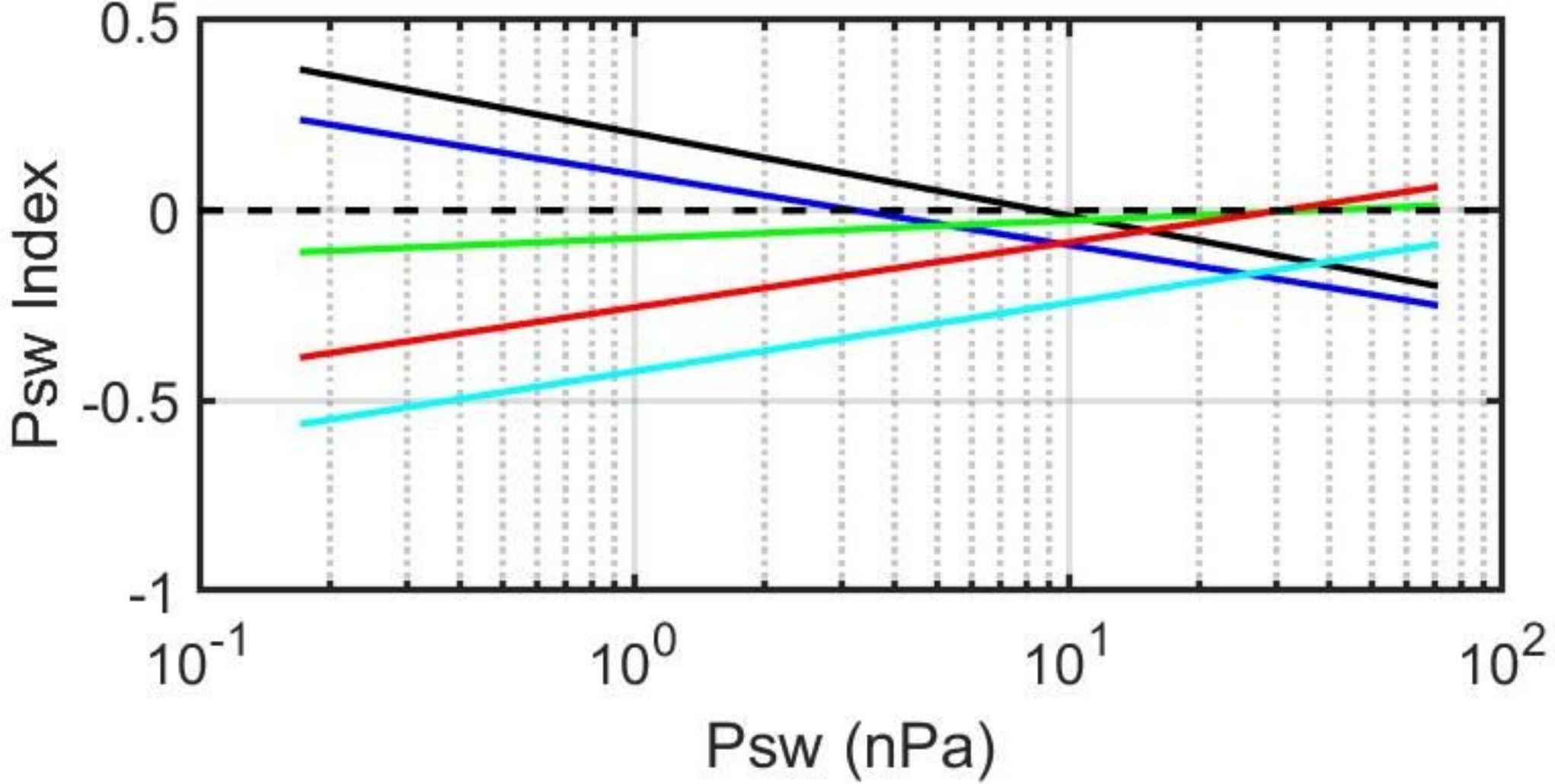


Figure 6.

